25th ABCM International Congress of Mechanical Engineering
October 20-25, 2019, Uberlândia, MG, Brazil

COB-2019-2313
EXPERIMENTAL AND NUMERICAL EVALUATION OF CHURN AND SLUG AIR-WATER FLOW IN HORIZONTAL AND INCLINED PIPES

M. R. Oliveira
M. P. Lima
M. F. Martins
R. S. Martins
R. Ramos
Universidade Federal do Espírito Santo (UFES), 514, Fernando Ferrari Av., Vitória, ES 29075-910, Brazil
marciellyo.oliveira463@gmail.com, marcelplima@gmail.com, marcio.martins@ufes.br, ramonsmartins@gmail.com, ramosrogerio@hotmail.com

Abstract. *The present work aims to verify the performance of the Volume of Fluid (VOF) model on flow pattern characterization in inclined circular cross-section pipe. For this purpose, a* 42 *mm diameter tube with* 4.5 *m length was used in numerical and experimental tests involving two flow patterns: slug and churn. VOF multiphase flow model combined with* $k-\varepsilon$ *Realizable turbulence model and scalable wall function was set in the simulations, as well as specific parameters for temporal discretization, spatial discretization and, mesh refinement. The results of the simulations showed that in the slug regime, the liquid pistons were associated with a mixture of the upstream and downstream phases of the pistons, as well as higher velocity in front of the liquid mass. Comparing the experimental and numerical results, there were expressive similarities in the images of the flow patterns, especially regarding the length of the piston. For the churn regime, the results of the simulations also showed flow patterns similar to those obtained experimentally. The average behavior of both patterns was verified by a numerical parameter that represents the non-dimensional wall distance, revealing the piston's frequencies.*

Keywords:*: Air-water flow, Computational Fluid Dynamics, Volume of Fluid, Inclined pipe, Flow pattern.*

1. INTRODUCTION

Flow consisting of different phases exhibit a large variety of phenomena due to the complicated and diverse interaction between each phase. Gas-liquid mixtures, for instance, can assume different patterns depending on the operational conditions such as, for example, flow rate, pressure, gravity, inclination, system dimensions, and physical properties of each phase, as described by Oliveira (2009). These patterns of multiphase flow are found in a wide range of engineering applications, such as the screw pump, hydrocyclone separator, bubble columns and, plastic injection (Lim *et al.*, 2010).

For gas-liquid simulation where the phase's separation interface needs to be tracked, Volume of Fluid (VOF) is recommended, since it introduces a volume fraction equation to the algorithm that calculates the individual phase mass for each Eulerian control volume. Inside ducts, tracking interfaces between fluids play an important role in the detection of different flow patterns, which can suggest the occurrence of unstable flow regimes, such as slug flow. This flow pattern is characterized by a liquid mass with small bubbles that separates large bubbles from each other (Taylor bubbles) in a chaotic interaction. When turbulence reaches a higher level, the liquid piston is compromised, and Taylor bubbles fade away, giving place to a new pattern called churn flow (Schepper *et al.*, 2008).

Unlike the churn pattern flow, slug pattern flow results in large pressure fluctuations that can harm equipment and pipeline structures. Flow characteristics such as the length, frequency, and the pressure drop function of the phases is a way to characterizing the average behavior of churn and slug flow patterns. These parameters can be extracted from the CFD simulation results. Therefore, the objective of this study is to set up the VOF model to represent two flow patterns in a pipe: one inclined (slug) and one horizontal (churn). To validate the results of the simulations, a multiphase experiment was carried out.

2. MATERIAL AND METHODS

2.1 Multiphase flow loop

Clean water and air were used to perform the gas-liquid flow in the experimental unit (Fig. 1) comprising one compressor, one air tank, one air flowmeter, one water flowmeter, two valves, one separation tank, one pump, a y-joint, and a pressure transmitter. To provide the two-phase mixture, atmospheric air is compressed into an air tank from a 30 HP electric screw compressor, while water is supplied by a reservoir that feeds a 2 CV centrifugal pump. The volume flow rate of each phase is independently measured by the turbine flowmeters and its amount is controlled by two manual control valves located downstream the flow measuring elements. Leaving the independent lines, both phases are mixed in a simple y-joint, where the air flows inside the straight inlet and water come from the bottom, in the angled branch. To develop the mixing process and perform the flow pattern experimental analysis, the mixture flows inside a 2.9 m long straight tube before reaching the glass pipe of length 740 mm.

After the visualization section, the pressure was taken by a pressure transmitter, used to obtain data for the simulation boundary condition. Finally, air and water were separated at the original reservoir that feeds the pump. All the straight pipe along which the phases flow has 42 mm in internal diameter and it can be inclined according to the need due to a central joint. To ensure flexibility at the inlet and outlet of the straight pipe, hoses were used.

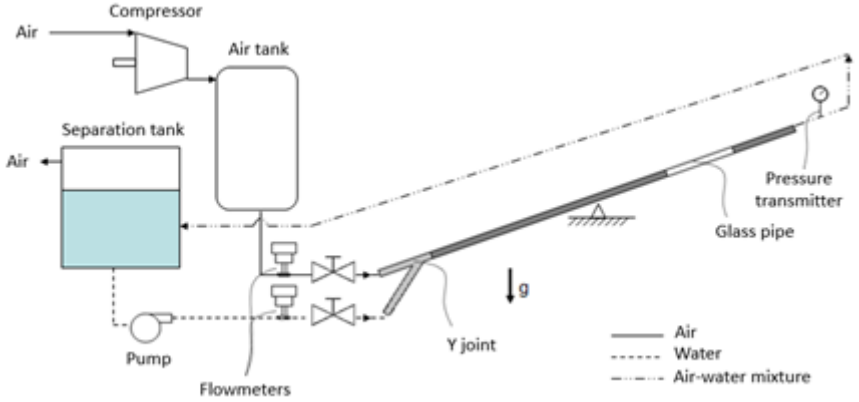

Figure 1: Multiphase flow loop

2.2 Experimental procedures

In the multiphase flow loop, two experiments were performed by computing the outlet pressure from pressure transmitter, as well as water and air volume flow rate from flowmeter devices, connected to a LabView software.

For each of the experiments, both control valves were set to the closed position before pressurizing the system. First, the centrifugal pump was activated, rising water pressure to the pump shutoff head, which decreases as water flow rises (by gently opening the control valve) until its flow rate reaches the desired value. Unlike the pump, no manual activation is necessary for the compressor, since an automatic system switches on and turns off the equipment to keep the right pressure inside the air tank.

Once all the loop piping was filled with water, the air control valve was slowly opened to set the airflow rate previously calculated for the experiment. Since the additional airflow increases the pressure drop inside the pipe, the system head curve changes, leading to a different pump flow rate, which must be adjusted after the mixture is established. The flow pattern image was collected by the camera taking photographies at the glass section of the tube.

Once the flow patterns were selected to be performed, the inclination and phases flow rate were obtained from Xu *et al.* (2007) flow pattern maps respecting the loop limitations. Table 1 shows these setups for each of the flow pattern, as well as the outlet manometric pressure obtained from the experiments (used as input data to the simulation boundary condition).

Table 1: Experiments setup and result outlet pressure.

Flow patter	**Inclination angle** ($^\circ$)	**Fluid**	**Flow rate** (m^3/h)	**Mean man. pressure (bar)**
Slug	15 (upward)	Water	9.98	4.5
		Air	3.49	
Churn	0	Water	19.95	5.5
		Air	3.49	

3. NUMERICAL MODELING

Volume of Fluid model (VOF) is based on Eulerian-Eulerian approach and it has vast application of gas-liquid flow simulation. In this model (Hirt and Nichols, 1981), both phases share the same transport equations. The continuity and momentum transport are described by the following equation, respectively:

$$\frac{\partial \varrho}{\partial t} + \nabla.(\varrho \overrightarrow{v}) = 0 \tag{1}$$

$$\frac{\partial}{\partial t}(\varrho \overrightarrow{v}) + \nabla.(\varrho \overrightarrow{v} \overrightarrow{v}) = -\nabla p + \nabla.\mu(\nabla \overrightarrow{v} + \nabla \overrightarrow{v}^T) + \varrho \overrightarrow{g} \tag{2}$$

where t is the time, ϱ is the fluid density, $\overrightarrow{v}$ is the average velocity vector, p is the pressure, μ is the effective viscosity and $\overrightarrow{g}$ is the gravity.

To solve phases volume fraction, VOF includes the continuity equation weighted by such fraction:

$$\frac{\partial(\propto_q \varrho_q)}{\partial t} + \nabla.(\propto_q \varrho_q \overrightarrow{v}) = 0 \tag{3}$$

where $\propto_q$ and ϱ_q are respectively the volume fraction and the fluid density of phase q present in the cell. This equation express that the transient nature of the interface is due is only to advective effects, disregarding completely the diffusive term and the need to consider any viscous effect. It is in accordance with the observation that the interface is not supposed to diffuse among several volume layers By solving Eq. 3, the phases separation interface is obtained where each $\propto$ reaches a value between 0 and 1.

By integrating the governing equations (Eq. 1, Eq. 2 and Eq. 3) on each of the small control volumes and applying the divergence theorem on the divergent terms of the equation, variables on the face of these control volumes shall appear. As a result, these variables must be interpolated (by upwind methods) from the face to the center of each control volume, so the solution can arise.

Among the interpolation methods available on Fluent®, first-order and second-order upwind are the most used in general application. Although the first one results in good iteration stability, whereas the second one performs more precisely (except in high gradient regions). Therefore, the spatial discretization was started using first-order upwind and then switched to second-order.

Although the VOF approach is useful for identifying the phases separation interface, it is not enough to determine the interface's shape. Further, the usage of conventional spatial interpolation methods (upwind) on such interface leads to a reduction of the volume fraction gradient, resulting in a diffuse interface (without clear segregation between phases). To solve this problem, many methods have been developed for interpolating the interface between phases: geometric reconstruction, donor-acceptor, compressive interface capturing scheme for arbitrary meshes (CICSAM), high-resolution interface capturing (HRIC), etc.

In their study, Jabbari *et al.* (2014) show that among HRIC, geometric reconstruction, and CICSAM, the first one shows the best combination of precision and computational cost, especially for free surface flow with non-Newtonian fluid. However, for Newtonian fluid, HRIC and CICSAM lead to the same result, meanwhile, geometric reconstruction differs both, giving the best result compared to experiments.

Temporal discretization can be performed with an explicit and implicit method. The first one gives the future value of a variable by only calculating its actual value. The second, instead, calculate the future information by an iteration process with actual and future values. Although the explicit method is less computationally expensive, it can result in the calculation instability when the time steps (Δt) or the flow velocity (u) are too high concerning the mesh size (Δx). Mathematically, Courant-Friedrichs-Lewy (CFL) must be:

$$CFL = \frac{|u|_0 \Delta t}{\Delta x} < 1 \tag{4}$$

After discretization by the finite volume method, the order of accuracy for the spatial and temporal derivative is chosen. Fluent® software provides two solution methods: Pressure-Based and Density-Based. Compressible flow can be simulated by using the continuity equation to calculate density, which associated to temperature gives the pressure field by state equation. However, the momentum equation solution becomes more complicated since there is no independent equation for pressure. Furthermore, this equation has no analytical solution yet, then the linearization and iteration processes are necessary. In the Pressure-Based method, the pressure field is obtained from the so-called pressure correction equation (from the manipulation of momentum and continuity equations), which can be solved separately from velocity

field calculation (Pressure-Based Segregated) or in a coupled equation system with velocity field (Pressure-Based Coupled). This last one shows a faster convergence process, although it is more computationally expensive. For transient simulation, this higher computational cost produces higher calculation time, then the segregated method seems to be more indicated with its PISO or FSM algorithms. Unlike FSM, PISO algorithm (Pressure-Implicit with Splitting of Operators) show better stability for multiphase flow simulations. In this process, PISO performs two additional corrections, which avoid the need for velocity recalculation until momentum balance is satisfied in SIMPLE or SIMPLEC algorithms.

Just like laminar flow, governing equations for turbulent includes Navier-Stokes and continuity equations. However, its inherent random state of motion for velocity and pressure (Taylor and von Karman (1937); Hinze (1975)) results in the need of high mesh refinement to simulate the whorls in small Kolmogorov's scale. This highly computationally expensive approach, known as Direct Numerical Simulation (DNS), can be replaced by performing the Reynolds decomposition method to the governing equations, which computes velocity and pressure as the sum of its mean value with its fluctuation over time, giving the governing equations (for Newtonian fluid and incompressible flows):

$$\frac{\partial \bar{u}_i}{\partial x_i} = 0 \tag{5}$$

$$\frac{\partial \bar{u}_i}{\partial x_i} + \bar{u}_j \frac{\partial \bar{u}_i}{\partial x_j} = \frac{1}{\varrho} \frac{\partial}{\partial x_j} \left[-\bar{p}\delta_{ij} + \mu \frac{\partial \bar{u}_i}{\partial x_j} - \varrho(\overline{u_i' u_j'}) \right] + g_i + \frac{1}{\varrho} S_i \tag{6}$$

where $\bar{u}$ is the average velocity, $\bar{p}$ is the average pressure, u' is the velocity fluctuation and, S is the source term.

Equation 6 is known as Reynolds Averaged Navier-Stokes. One might note that this equation shows a new term (in relation to Eq. 2) as function of velocity fluctuation, introducing six new variables to the system, such term is known as Reynolds tensor: $\tau_{ij} = \varrho(\overline{u_i' u_j'})$. To avoid this additional computational cost, the Boussinesq hypothesis was used by replacing the velocity fluctuation term to a function of the mean velocities, turbulent viscosity, and turbulent kinetic energy. This approach is used in the Spalart-Allmaras, $k-\varepsilon$ and $k-\omega$ models.

For lower Reynolds number, $k-\varepsilon$ Realizable is generally the most recommended $k-\varepsilon$ model in Fluent®, it considers turbulent viscosity as isotropic and it differs from the others by satisfying certain mathematical constraints on the Reynolds tensor, consistent with the physics of turbulent flows. The turbulent viscosity (μ^T) is calculated using the Eq. 7.

$$\mu^T = C_\mu \frac{k^2}{\varepsilon} \tag{7}$$

where k is the turbulent kinetic energy, ε is its rate of dissipation and C_μ is a constant . In the $k-\varepsilon$ model, the k and ε are calculated using the Eq. 8 and Eq. 9 respectively:

$$\frac{\partial \varrho \varepsilon}{\partial t} + \nabla . \left[\varrho \overrightarrow{v} \varepsilon - \left(\mu + \frac{\mu^T}{\sigma_\varepsilon} \right) \nabla_\varepsilon \right] = C_1 \frac{\varepsilon}{k} P^k - C_2 \varrho \frac{\varepsilon^2}{k} \tag{8}$$

$$\frac{\partial \varrho k}{\partial t} + \nabla . \left[\varrho \overrightarrow{v} k - \left(\mu + \frac{\mu^T}{\sigma_k} \right) \nabla_k \right] = P^k - \varrho \varepsilon \tag{9}$$

The constants values used in the simulations were C_1 = 1.44, C_2 = 1.92, σ_k = 1.0, σ_ε = 1.3 and C_μ = 0.09 (Jaeger *et al.*, 2018). The turbulence production P^k is obtained from Eq. 10.

$$P^k = \mu^T (\nabla \overrightarrow{v} + (\nabla \overrightarrow{v})^T) : \nabla \overrightarrow{v} \tag{10}$$

The turbulent kinetic energy dissipation in the Realizable $k-\varepsilon$ model is expressed as:

$$\frac{\partial \varrho \varepsilon}{\partial t} + \nabla . \left[\varrho \overrightarrow{v} \varepsilon - \left(\mu + \frac{\mu^T}{\sigma_\varepsilon} \right) \nabla_\varepsilon \right] = C_1 \varrho S \varepsilon - C_2 \varrho \frac{\varepsilon^2}{k + \sqrt{v\varepsilon}} \tag{11}$$

where S is the mean rate-of-strain tensor.

As described by Jaeger *et al.* (2018), one feature of this model is that ε does not use the turbulent kinetic energy production. Another characteristic is that the destruction term does not reach any singularity when k becomes null. C_1 is calculated using the following equations:

$$C_1 = max\left(0.43; \frac{\eta}{\eta + 5}\right) \tag{12}$$

$$\eta = \frac{Sk}{\epsilon} \tag{13}$$

Whether for laminar or turbulent flow, the velocity gradient is observed close to the wall due to no-slip condition, leading to the need for better mesh refinement at this zone. Additionally, velocity fluctuation in turbulent flow is also influenced by viscosity effects in the boundary layer, which must be considered in the simulation (Dewan, 2011). Fortunately, for high Reynolds number flow, the non-dimensional velocity profile remains the same inside the boundary layer, in which velocity is a function of the distance from the wall, calculated differently at the viscous sub-layer and the turbulent sub-layer. Wall functions can be performed to calculate the velocity close to the wall, resulting in less computational cost and low mesh refinement.

Fluent ® software includes four wall functions: Standard, Scalable, Non-Equilibrium, and Enhanced. This last one requires higher mesh refinement than the others and the third one is more indicated for simulating detachment of the boundary layer. In Standard and Scalable wall function, velocity is obtained from the turbulent sub-layer equation for $y^* > 11.22$. This non-dimensional variable indicates the minimum distance from the wall and it can be calculated by the Eq. 14.

$$y^* = \frac{\varrho C_\mu^{1/4} k_P^{1/2} y_P}{\mu} \tag{14}$$

where y_P is the distance between the wall and the center of its adjacent cell, and k_P is the turbulent kinetic energy at the center of this cell.

For $y^* < 11.22$, Standard wall function calculates velocity from the viscous sub-layer equation, which deteriorates numerical results for $y^* < 11$. This problem is avoided by Scalable wall function since y^* minimum value is limited to 11 and viscous sub layer equation is only applied for $11 < y^* < 11.22$.

Although turbulent kinetic energy (k) and its dissipation rate (ε) are calculated from transport equation in Standard and Scalable wall functions, the calculation of ε at the cells adjacent to the wall is performed by the Eq. 15.

$$\varepsilon_P = \frac{C_\mu^{3/4} k_p^{3/2}}{\kappa . y_P} \tag{15}$$

where κ is the von Kármán constant.

3.1 Simulation setup

Fluent ® v.14 software was used in a 10 cores cluster computer with Linux v.$3.11.0 - 26$-generic operational system, Intel Xeon CPU $E5 - 2670$ v2 @ 2.50GHz processors and a 32 GB RAM.

Since the presence of dispersed phase does not characterize the flow patterns simulated, the Euler-Euler approach was used with the VOF model (indicated for tracking the phases separation interface), performing geometric reconstruction discretization for volume fraction. $k - \varepsilon$ Realizable model was applied for obtaining turbulence effects, with a Scalable wall function (which combines calculation stability and accuracy for relatively low refined mesh in a no boundary layer separation flow). Such function avoids instabilities in a low y^+, which might occur at low-velocity regions in slug flow, e.g. due to great velocity variations.

All the calculations were performed with: PISO algorithm including a maximum of 10^{-6} in scale residual and time step number below 60. The implicit time discretization with a CFL of 0.8 was used due to its better numerical stability (although no numerical instability might be observed in the implicit approach for CFL higher than 1, phases interface dissipation was observed for this higher values).

The spatial discretization of the momentum equation was performed by using the first-order upwind method for the first time steps (around the initial 500 one), followed by the use of the second-order upwind method for the rest of the calculations. Due to the attenuation of the volume fraction gradient at the phase interface caused by the upwind spatial discretization methods, geometric interpolation was used, which can generate interface contours with better accuracy than other methods (ANSYS, Inc, 2011). For the spatial discretization of turbulent kinetic energy and its dissipation rate, first-order upwind was chosen due to numerical instabilities caused by the second-order upwind in preliminary tests in simulated regimes.

Boundary conditions included constant inlet phases flow rate, gravitational force inclination as well as constant outlet pressure obtained from experiments (Tab. 1). Since the k-ε turbulent model was used, k and ε would be also set in the boundaries. However, difficulties on direct measurement of these parameters, turbulent intensity I and hydraulic diameter L were set instead. k, ε, I and L are related by the following equations:

$$I = \frac{\sqrt{\frac{2}{3}k}}{\bar{u}} \tag{16}$$

$$\epsilon \approx \frac{\bar{u}^3}{L} \tag{17}$$

According to ANSYS, Inc (2011), the turbulent intensity can be estimated by the following equation:

$$I = 0.16Re^{-1/8} \tag{18}$$

where Re is the Reynolds number and $\bar{u}$ is the mean flow velocity.

3.2 Mesh evaluation

For the wall boundary condition, it has been considered a no-slip condition and null k gradient in the normal direction.

Once the simulation setup and the flow domain geometry are defined, a mesh test was performed to obtain the best simulation result with the lower number of cells as possible. This approach allows less computational cost combined with enough agreement to the experimental results.

Four unstructured meshes were tested: Mesh 1 (881.854 cells), Mesh 2 (956.861 cells), Mesh 3 (1.029.237 cells) and Mesh 4 (1.313.585 cells). Figure 2 shows the longitudinal cross-sectional views of the Y region for each mesh in which the distributions of the gray-scale phases are presented. In the figure might observe the air flow interacting with the water flow forming a separation interface whose shape can be compared to identify the mesh of coarser elements such that the interface tends to remain the same for greater mesh refinements (ideal mesh). Figure 3 shows the graph generated which was used to evaluate the degree of similarity between the interfaces of the phases for the different meshes, which presents an interface with a format for each mesh according to the referential shown in Fig. 2. From the Fig. 3, it is possible to perceive that, as more refinement of the mesh is carried out, separation interfaces are generated more similar to the one generated with the most refined mesh (Mesh 4), so that the Mesh 3 already presents interface with format very similar to that presented by Mesh 4. In other words, extreme refinements tend to produce more computational cost than accuracy, for this reason, mesh 3 was used in the simulations.

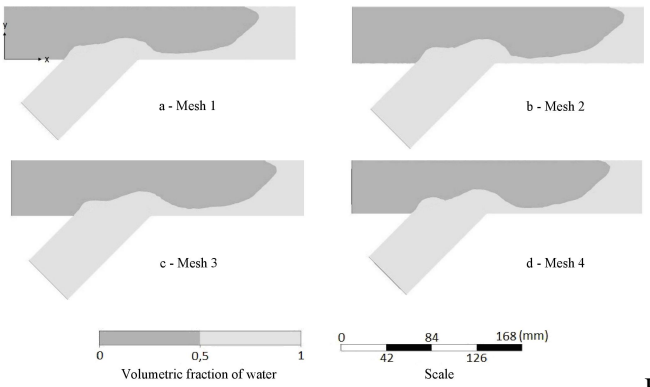

Figure 2: Phase Separation Interfaces at the y-joint

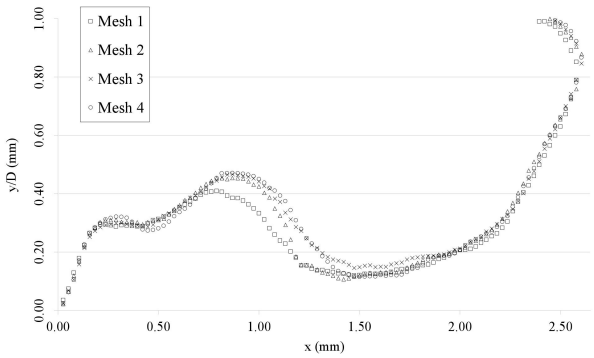

Figure 3: Shapes of phase's separation interface at y-joint for different mesh refinements

To homogenize the distance from the wall to the center of its adjacent cells, inflation method was applied to Mesh 3, comprising 3 cells layers with radial a length growth ratio of 20% and radial length at the cell adjacent to the wall of 0.225 mm.

With this new mesh (Mesh 3a), a preliminary slug regime simulation was performed giving a maximum y^+ of 50. Since the use of wall function for turbulence allows the use of y^+ between 50 and 500 (Bakker, 2006), inflation in Mesh 3a seems to be too refined so a coarser mesh (Mesh 3b) was generated with a new radial length at the cell adjacent to the wall:

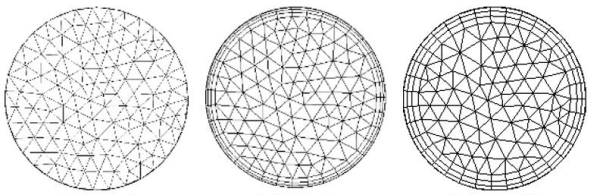

Figure 4: Mesh 3, Mesh 3a and Mesh 3b cross sections

4. EXPERIMENTS

Through manual control of the valves of the air-water circuits, associated with the visual monitoring of the flowmeter indication, the slug regime was obtained at 15^{o} forward flow direction concerning the horizontal plane. Figure 5 shows the visual results obtained by photos in the display region for the slug flow with the temporal evolution of 0.38 s between each consecutive image. The values of the phase flow for this regime (Tab. 1) coincide with those tested by Xu *et al.* (2007) for a 40 mm inner diameter tube, which in turn indicates the establishment of the same regime obtained experimentally in the present work. This correspondence between the results of the experiment and that presented in the literature points to a convergence of the procedures adopted in both studies, especially for the values of flow indicated by the meters and the slope imposed on the straight section.

Figures 5-a and 5-e show the passage of a slug liquid piston comprising the entire diameter of the tubing and flowing at a high velocity relative to the liquid film between two pistons (Fig. 5-b). Additionally, as described by Dukler and Hubbard (1975), the front of the piston presents a chaotic mixture of phases, explained by the acceleration imposed on the film. In Fig. 5-c and 5-d, on the other hand, it is possible to perceive characteristics of the liquid film soon after the passage of the piston, whose agitation and acceleration caused in the liquid mass result in mixing the phases which extend until the first instants of the formation of the liquid film. In these figures, the phase separation interface still encounters gas bubbles which will gradually die out until further agitation in the passage of the next piston. The intermittent flow of the pistons (characteristic of slug flows) is verified by observing the consecutive images that sometimes confirm the presence of the piston, sometimes show flow with the low amplitude wave interface.

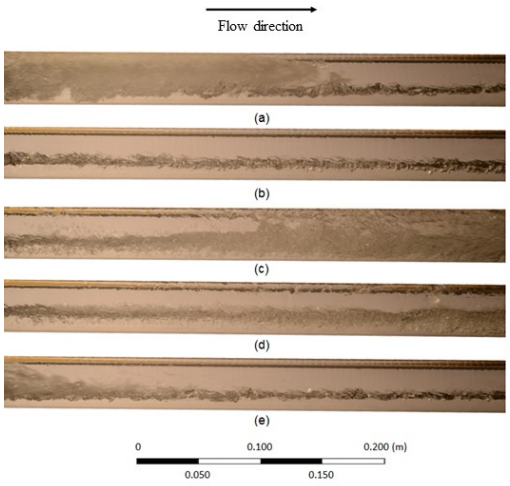

Figure 5: Experiments of slug flow

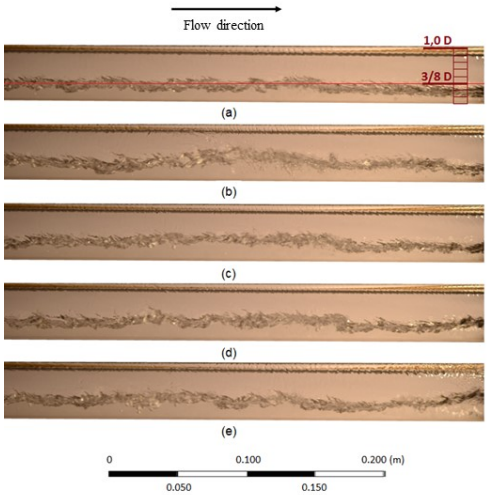

Figure 6: Experiments of churn flow

With the increase of the gas fraction in the mixture in relation to the slug experiment and in the absence of sloping concerning the horizontal plane, the churn flow was obtained, as can be seen from the Fig. 6. The images were photographed in the time interval used to obtain the photographies of slug flow. The values of the flows of each phase are presented in Tab. 1, coinciding with one of the experiments performed by Xu *et al.* (2007) for the churn regime.

From the images of Fig. 6, undulations are observed at the phase separation interface so that their amplitudes are insufficient for complete filling of the cross-section of the pipeline and are not capable of forming the liquid pistons. Through this observation, it can be suggested that the presented flow belongs to one of the three horizontal flow regimes: wavy (by the presence of corrugated water film), churn (with the discontinuity of liquid pistons caused by) or annular (by high gas flow). After some verifications and calculations, the hypothesis of wave and annular flow patterns were discarded. Therefore, the flow reproduced in the laboratory leads to the assertion that such a regime was formed by the breaking of the liquid pistons with their high volumetric fraction of gas ($\alpha_s > 0.58$).

5. RESULTS AND DISCUSSION

The numerical results of the two regimes reproduced in the experiments were obtained with a total number of time steps and physical time of 62000 and 1.96 s, and 60000 and 1.41 s for slug and churn respectively. The residuals of k and ε equations remained lower than 10^{-6} at the end of the iterations of each time step for churn pattern, whereas for slug pattern only the residuals of k equation and velocity reach such criteria. The continuity equation presented slower convergence, resulting in a residue of the order of 10^{-5} at the end of each time step.

As suggested by the images of the numerical experiment in the slug pattern (Fig. 7), the simulation result showed a flow with specific characteristics of this pattern. In the figure, pistons of amplitude equal to the diameter of the pipe and with intermittent passages were identified along its longitudinal section, as presented by the color scale of volumetric fraction of water.

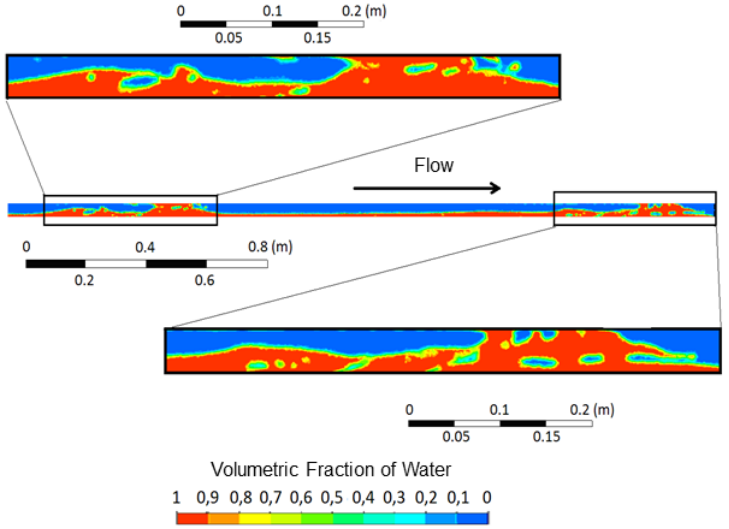

Figure 7: Color map of the volumetric fraction of water in the longitudinal section of the tube

Additionally, according to Dukler and Hubbard (1975), liquid pistons are typically faster than the flow established between the passage of consecutive pistons. Numerically, such characteristic could be observed based on the velocity map in a straight section with the presence of a piston (Fig. 8-a) and after its passage (Fig. 8-b). In both figures, the gray-scale indicates the volumetric fraction of each of the phases, being light grey to 100 % water and dark gray to 100 % air. Note that the speed of the front of the piston is about 10 m/s, while, after its passage, the velocity in the axis of the tube assumes values around 3.5 m/s.

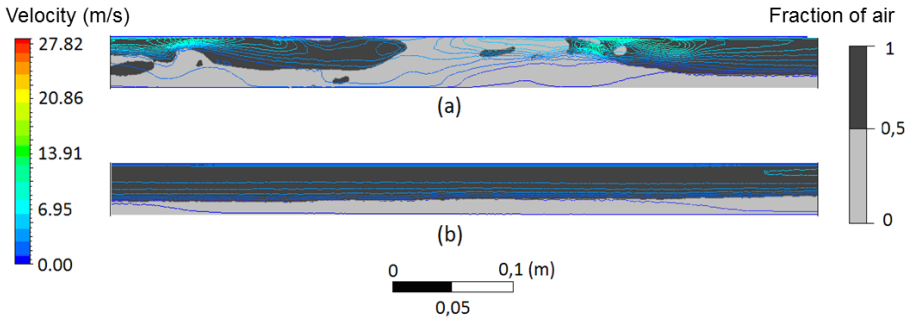

Figure 8: Color map of the volumetric fraction of water in the longitudinal section of the tube

According to Dukler and Hubbard (1975), the velocity variations caused by the passage of the liquid pistons into the flow lead to the generation of chaotic piston mixtures which can be seen in Fig. 9 (where numerical and experimental results are compared), also from the Fig. 9, it is possible to perceive similarities between the pistons, such as their length of about 12.2 cm and the occurrence of the chaotic mixture upstream and downstream them.

The numerical result obtained for the churn flow is shown in Fig. 10. Note that, the presence of undulations along the tubing, as well as in the experiment (bottom part of the figure); in addition, the model was capable of tracking the regions of mixing of air and water due to strong agitation that is an inherent characteristic of this flow pattern.

Finally, as the numerical results make possible extrapolate average parameters governing both flow patterns, an important parameter can be used to qualify the fluid dynamics behavior of flow patterns, that is, y^+. This non-dimensional

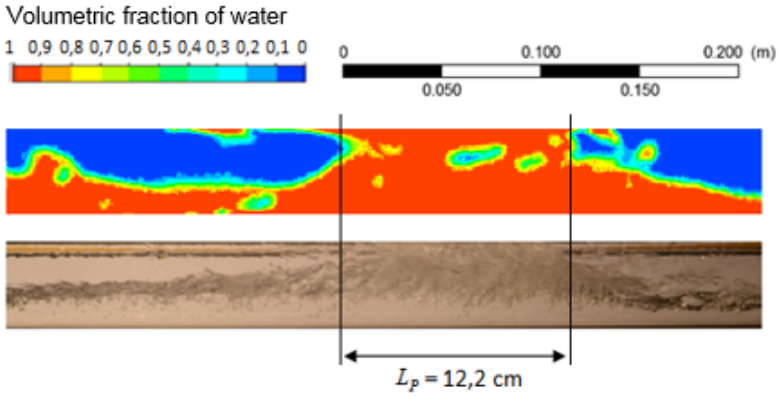

Figure 9: Color map of water volume fraction and photograph of the experiment for slug pattern

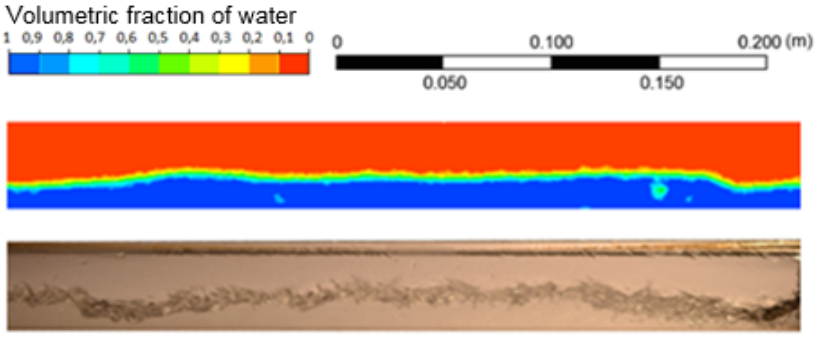

Figure 10: Color map of water volume fraction and photograph of the experiment for churn pattern

wall distance, for a wall-bounded flow, can be used to track flow variations if plotted along the pipe length.

Figure 11 and 12 show, for simulated slug and churn pattern respectively, the distribution of values for all cells touching the tube wall along its length from the water inlet section at y-joint to the output region of the straight section (represented by the "x" axis of the graphics). The simulation time instants shown in the graphs are the same as those used in Figures 9 and 10 for the same simulated flow rates.

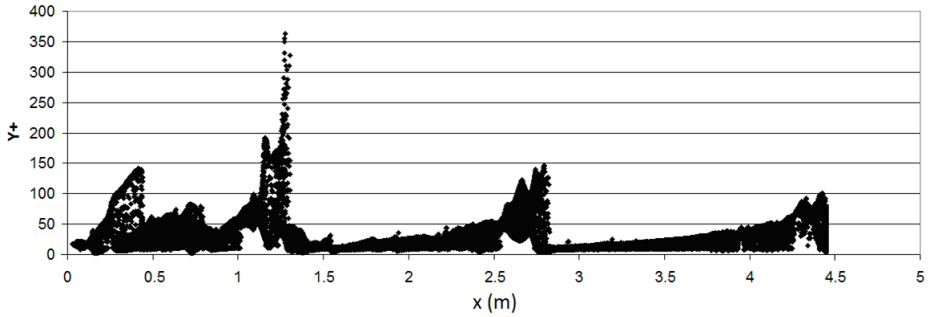

Figure 11: Distribution of y^+ along the tube for slug pattern

Some particular characteristics of each flow pattern can be seen in their respective graphs. The result for the slug pattern leads to y^+ peaks which coincide with the passage of the characteristic pistons inherent to this flow pattern. Higher shear stresses in the fluid caused by the piston flow at high speed promote an increase in the values of y^+, generating the peaks in the graph. The abrupt rise of y^+ upstream of the piston is followed by its gradual reduction, characterized by the stirring left of the phase separation interface downstream of the piston.

From Fig. 12, elevations in y^+ values along the pipe length are identified, which must be related to the inherent disturbances of churn flow.

Based on the Fig. 11 and Fig. 12, it is notorious that the distribution of y^+ values is between 0 and 500 for both patterns, therefore, the condition of Bakker (2006) is satisfied, as well as the mechanism of non-deterioration of the calculations presented by Scalable Wall Function for cells with $0 < y^+ < 50$.

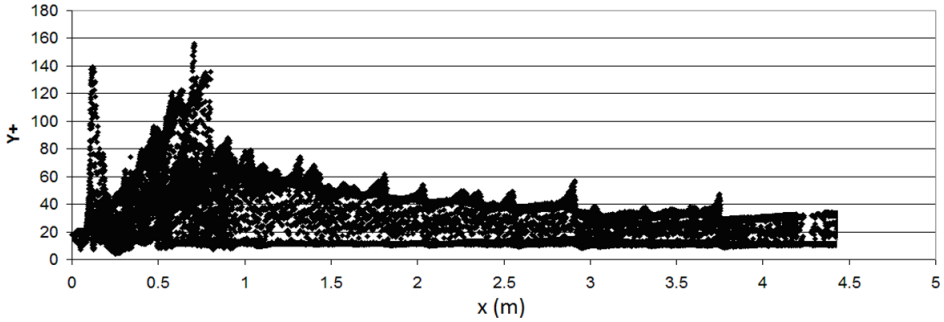

Figure 12: Distribution of y^+ along the tube for churn pattern

6. CONCLUSIONS

The results of the simulations showed flow characteristics compatible with the predicted regimes. In the slug regime, the liquid pistons were associated with a mixture of the upstream and downstream phases of the pistons, as well as the higher velocity in front of the liquid mass, as described by Dukler and Hubbard (1975). Comparing the experimental and numerical results, there were expressive similarities in the images of the flow patterns, especially with regard to the length L_p (Fig. 9) of the piston. For the churn regime, the results of the simulations also showed flow patterns similar to those obtained experimentally. The smaller wave scales perceived in the practical experiments were not caught in the numerical results, which, according to ANSYS, Inc (2011), is expected for models based on the RANS equation as k - ε Realizable. In addition, the degree of refinement of the mesh may also have contributed to the relatively low resolution of the undulations at the phase separation surface and in the regions of chaotic mixing of the slug regime, since better resolution was achieved by Hua *et al.* (2015) with the use of the model k - ε Standard. However, the average behavior of both patterns could be qualified by a numerical parameter such as non-dimensional wall distance revealing piston frequency.

7. REFERENCES

ANSYS, Inc, 2011. *Ansys Fluent Theory Guide. Canonsburg: ANSYS, 2424p.* URL `https://www.ansys.com`.

Bakker, A., 2006. "Lecture 11 – boundary layer and separation – applied computational fluid dynamics - slides".

Dewan, A., 2011. *Tackling Turbulent Flows in Engineering*. Springer. ISBN 978-3-642-14766-1.

Dukler, A.E. and Hubbard, M.G., 1975. "A model for gas-liquid slug flow in horizontal tubes". *Industrial & Engineering Chemistry Fundamentals*, Vol. 14. doi:10.1021/i160056a011.

Hinze, J.O., 1975. *Turbulence*. New York, N.Y. : McGraw-Hill, 2nd edition. ISBN 0070290377.

Hirt, C. and Nichols, B., 1981. "Volume of fluid (vof) method for the dynamics of free boundaries". *Journal of Computational Physics*, Vol. 39, No. 1, pp. 201 – 225. ISSN 0021-9991.

Hua, J., Nordbø, J. and Foss, M., 2015. "Cfd modelling of gas entrainment at a propagating slug front".

Jabbari, M., Bulatova, R., Hattel, J. and Bahl, C., 2014. "An evaluation of interface capturing methods in a vof based model for multiphase flow of a non-newtonian ceramic in tape casting". *Applied Mathematical Modelling*, Vol. 38, No. 13, pp. 3222 – 3232.

Jaeger, J., Santos, C., Rosa, L., Meier, H. and Noriler, D., 2018. "Experimental and numerical evaluation of slugs in a vertical air–water flow". *International Journal of Multiphase Flow*, Vol. 101, pp. 152 – 166. ISSN 0301-9322.

Lim, E.W.C., Chen, Y.R., Wang, C.H. and Wu, R.M., 2010. "Experimental and computational studies of multiphase hydrodynamics in a hydrocyclone separator system". *Chemical Engineering Science*, Vol. 65, No. 24, pp. 6415 – 6424. ISSN 0009-2509.

Oliveira, R.P., 2009. "Caracterização experimental das propriedades dinâmicas de escoamentos pistonados em tubos verticais. 135 f. dissertação (mestrado em engenharia mecânica)".

Schepper, S.C.D., Heynderickx, G.J. and Marin, G.B., 2008. "Cfd modeling of all gas–liquid and vapor–liquid flow regimes predicted by the baker chart". *Chemical Engineering Journal*, Vol. 138, No. 1, pp. 349 – 357.

Taylor, G.I. and von Karman, T., 1937. "Turbulence". *The Journal of the Royal Aeronautical Society*, Vol. 41, No. 324, p. 1109–1143.

Xu, J., xiang Wu, Y., hong Shi, Z., yun Lao, L. and hui Li, D., 2007. "Studies on two-phase co-current air/non-newtonian shear-thinning fluid flows in inclined smooth pipes". *International Journal of Multiphase Flow*, Vol. 33, No. 9, pp. 948 – 969.

8. RESPONSIBILITY NOTICE

The authors are the only responsible for the printed material included in this paper.